Unveiling the Multifunctional Carbon Fiber Structural Battery

ADVANCED MATERIALS
www.advmat.de

Unveiling the Multifunctional Carbon Fiber Structural Battery

Richa Chaudhary, Johanna Xu, Zhenyuan Xia, and Leif E. Asp**

Structural batteries refer to the multifunctional device capable of both storing electrical energy and bearing mechanical loads concurrently. In this context, carbon fibers emerge as a compelling choice of material and serve dual purpose by storing energy and providing stiffness and strength to the battery. Previous investigation has demonstrated proof-of-concept of functional positive electrodes against metallic lithium in structural battery electrolyte. Here, an all-carbon fiber-based structural battery is demonstrated utilizing the pristine carbon fiber as negative electrode, lithium iron phosphate (LFP)-coated carbon fiber as positive electrode, and a thin cellulose separator. All components are embedded in structural battery electrolyte and cured to provide rigidity to the battery. The energy density of structural battery is enhanced by use of the thin separator. The structural battery composite demonstrates an energy density of 30 Wh kg^{-1} and cyclic stability up to 1000 cycles with ≈100% of Coulombic efficiency. Remarkably, the elastic modulus of the all-fiber structural battery exceeds 76 GPa when tested in parallel to the fiber direction – by far highest till date reported in the literature. Structural batteries have immediate implication in replacing structural parts of electric vehicles while reducing the number of conventional batteries. Thus, offering mass savings to future electric vehicles.

1. Introduction

A multifunctional structural battery is an emerging concept in the field of electric power. Presently, lithium-ion batteries (LIB) are extensively employed for powering the devices such as electric vehicles and electric aircraft, due to their exceptional performance. Despite this, the energy density state-of-the-art of lithium-ion battery remains inadequate, limiting the range of electric transportation.[1] This can be overcome by developing structural electrodes with high specific capacity, extending the voltage window, and integrating the multifunctional battery in structure.[2] Along storing the electrochemical energy, the primary role of the multifunctional battery is to carry the applicable mechanical load and reduce the overall system weight, extending the driving range or the mileage.[3] Structural batteries offer potential to achieve weight savings of up to 20% by just replacing the roof of an electric vehicle with a structural battery.[4] This weight reduction allows for the installation of more batteries, thereby increasing the vehicle's mileage. Despite the importance of multifunctionality, little innovation in terms of structural power has been accomplished in the past few decades.

In this context, intermediate modulus polyacrylonitrile (PAN)-based carbon fibers (CF) stand out as best balance between mechanical and electrochemical properties.[5] The electrochemical cycling of these fibers is studied as negative electrode in structural batteries, while only few focused on positive electrodes but limited to the presence of liquid electrolyte system.[6] Electrophoretic deposition is used to coat the surface of CF with lithium iron phosphate ($LiFePO_4$, LFP).[7] Specific capacity of 100 mAh g^{-1} is reported, however the poor capacity retention of 47% after 100 cycles are seen. This confirms the weak bonding between the deposited LFP and CF in the EPD process, which can lead to poor capacity retention. When LFP is coated onto the CF surface, it forms an interface where the adhesion between the two materials is not strong enough. Consequently, during cycling (such as 100 cycles), the LFP particles may detach from the CF surface, leading to reduced capacity retention. Furthermore, the repeated volume changes of ca. 7% during the charging and discharging of lithium-ion batteries cause the LFP nanoparticles to lose contact with CF.[7] The performance of positive electrode is further improved by incorporating the reduced graphene oxide (rGO) with LFP.[6c,e] The performance of these composites is tested in a liquid electrolyte, resulting in a specific capacity of 72 mAh g^{-1} at a 2C-rate.[6c] Another, important parameter of maintaining the mechanical property after electrochemical cycling is confirmed. The mechanical properties of IMS65

R. Chaudhary, J. Xu, Z. Xia, L. E. Asp
Department of Industrial and Materials Science
Chalmers University of Technology
Hörsalsvägen 7B, Göteborg 41258, Sweden
E-mail: richac@chalmers.se; leif.asp@chalmers.se

R. Chaudhary, L. E. Asp
Department of Industrial and Materials Science
Wallenberg Initiative Material Science for Sustainability
Chalmers University of Technology
Hörsalsvägen 7B, Göteborg 41258, Sweden

The ORCID identification number(s) for the author(s) of this article can be found under https://doi.org/10.1002/adma.202409725

DOI: 10.1002/adma.202409725

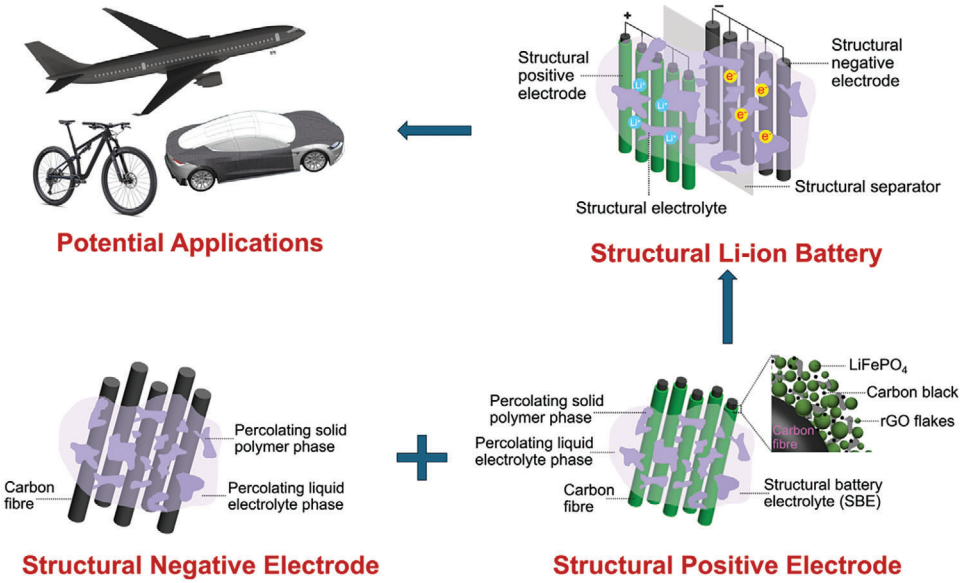

Figure 1. A detailed roadmap for the development and implementation of All-Fiber Structural Batteries.

and T800H CF are tested after 1, 10, 100, and 1000 cycles – no damage on the interface between the CF and coating is seen after 1000 cycles, which confirms a stable structure.[6d,8] Furthermore, the Young's modulus and energy density of structural battery using CF as current collectors and load-bearing components is studied.[9] Graphite is used for the anode, and $LiFePO_4$ (LFP) with carbon nanotubes (CNTs) for the cathode, coated on CF weave materials. A Whatman GF filter separator with an electrolyte of 1 M Lithium bis(trifluoromethane)sulfonimide (LiTFSI) in 1-Ethyl-3-methylimidazolium tetrafluoroborate (EMIMBF) is employed. The battery, sandwiched between epoxy-impregnated CF, showed an energy density of 36 Wh kg^{-1} and Young's modulus of 1.8 GPa.[9] Another approach on directly using uncoated carbon fibers as anodes material in structural battery and aluminum foil coated with LFP as cathode has been published.[10] Two types of separators are used and energy density with Whatman GF/A and plain weave separator is reported to be 12 and 24 Wh kg^{-1}, respectively. The performance difference was attributed to the greater thickness of the Whatman GF/A compared to the GF plain weave.[10] This increased thickness led to higher internal resistance, thereby reducing the maximum available capacities of the electrodes. The mechanical performance of structural battery is assessed in an in-plane tensile testing mode, reporting a Young's modulus of 18 and 25 GPa, parallel to the extension of carbon fibers in the negative electrode for Whatman GF/A and GF plain weave separator, respectively. Recently, the energy density of this type of structural battery has been enhanced to 42 Wh kg^{-1}, while maintaining the modulus, by an improved manufacturing technique.[6b] In addition, the energy density and Young's modulus of a battery based on carbon fiber have been examined in the context of a structural battery electrolyte. The structural battery laminate is manufactured using a vacuum-assisted infusion process with the biphasic solid electrolyte. The findings report an energy density of 33.4 Wh kg^{-1}, Young's modulus of 38 GPa, and a tensile strength of 234 MPa.[11]

Notably, all the mentioned methods come with few drawbacks such as being limited to the use of a liquid electrolyte, carbon fiber used only for negative electrode, or use of a commercial LFP foil as positive electrode, etc. Previous work by the authors has demonstrated the proof-of-concept of electrochemical and mechanical performance of structural positive electrode in half-cell configuration, using lithium metal foil as negative electrode.[12] However, the lithium metal cannot be used at industrial scale due to safety concerns such as high chemical activity, large volume changes, unstable solid electrolyte interphase (SEI), uncontrollable growth of Li dendrites, which can cause short-circuiting. Hence, it is of prime importance to validate these carbon fiber-based electrodes in full-cell configuration. Herein, an all-carbon-fiber-based structural lithium-ion battery is demonstrated in a structural battery electrolyte system (**Figure 1**). Pristine CF is used as negative electrode, LFP-coated CF as positive electrode, either cellulose/Freudenberg/Whatman as separator – all embedded in a bi-phasic solid-liquid structural battery electrolyte.

2. Results and Discussion

Multifunctional structural batteries have potential to become ubiquitous as a powering technique in future electric vehicles, in aerospace industries, and portable electronics. The main advantage of structural batteries is that they have been designed to combine inherent energy storage advantages (weight saving and enhanced structural integrity) with the advantage of multifunctionality. Multifunctionality is of prime importance, especially if one seeks to replace the electrochemically inactive components from lithium-ion batteries, reduce overall weight, and extend the mileage. Here, electrochemically active positive electrodes designed to achieve these innovations are tested in a full-cell configuration using structural battery electrolytes. Various thicknesses of separators are being investigated to develop lightweight structural batteries.

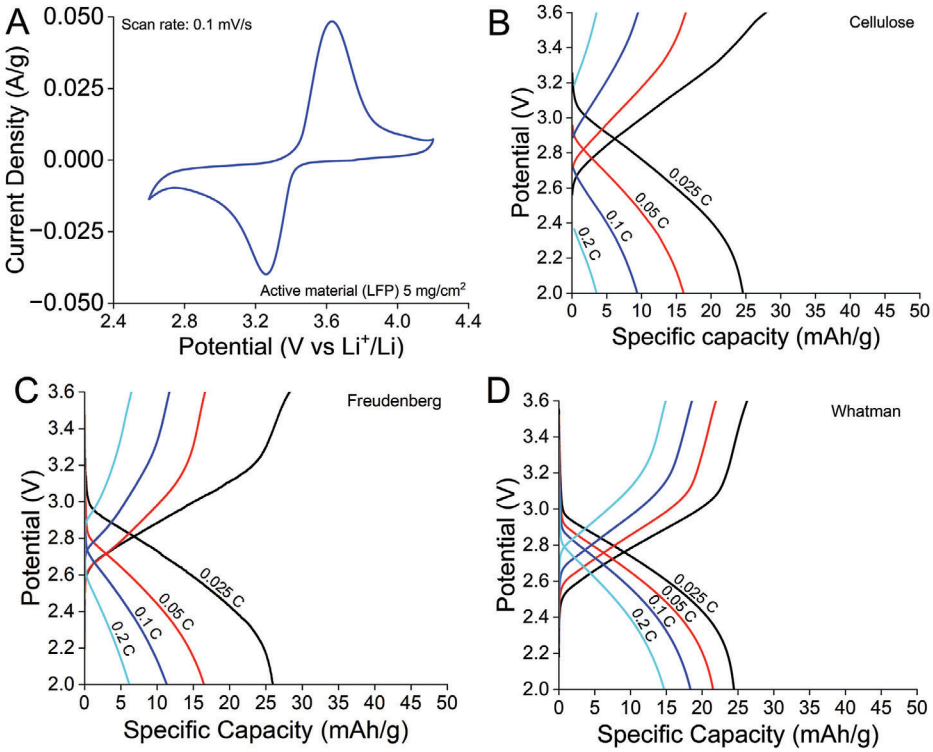

Figure 2. Electrochemical testing of all-fiber structural battery. A) Cyclic voltammetry of structural positive electrode. B–D) Specific capacity of full cell at varying C-rates with different separators. B) cellulose separator. C) Freudenberg separator. D) Whatman separator. Specific capacity relates to the mass of active materials to allow comparison of the full cell performances.

2.1. Proof-of-Concept of an All-Fiber Structural Battery is Demonstrated using Cellulose Freudenberg and Whatman Separator

The electrochemical stability and reversibility of faradic redox reaction of $LiFePO_4$ particles deposited on CF is tested by cyclic voltammetry in a half-cell configuration versus metallic lithium. **Figure** 2A illustrates a sharp and symmetric peak, with a small potential difference of 0.33 V between the anodic and cathodic peaks, confirming low polarization and high redox reversibility. Moreover, the structural battery electrolyte was found stable in this potential range, as no additional peak corresponding to electrolyte oxidation/reduction was observed. Following this initial confirmation of redox reversibility, a structural battery was fabricated using LFP-deposited CF as the positive electrode and pristine T800 CF as the negative electrode. Using a separator is essential to prevent a short circuit between positive and negative electrodes, but it typically increases the weight and thickness of the battery without contributing to the electrochemical reaction. Therefore, a primary objective is to identify the thinnest separator while optimizing porosity for ion migration. Here, three different separators – cellulose, Freudenberg with a glass fiber veil, and Whatman – are tested in a structural battery (Table S1, Supporting Information). All components are fabricated using a LiTFSI-based structural battery electrolyte and undergo galvanostatic cycling within a potential range of 2–3.6 V. Each of the three cells with different separators demonstrated a specific capacity of 25 ± 2 mAh g^{-1} at a 0.025C rate (Figure 2B–D). However, an increase in the C-rate resulted in a decrease in specific capacity due to the rapid migration of lithium. The structural battery, when using Whatman as a separator, displayed satisfactory performance up to a 0.2C rate, attributed to its high porosity.

The specific capacity of structural positive electrodes has been recently shown to be 95 mAh g^{-1} at a 0.05C rate in a half-cell setup with a similar active material loading. This value significantly drops to 25 mAh g^{-1} for a full cell, possibly due to the limited availability of lithium and the lower ionic conductivity of the structural battery electrolyte. The ionic conductivity of the structural positive electrode is reported to be 7.4×10^{-4} S cm^{-1}, which is ten times less than a traditional liquid electrolyte system.[12]

Moreover, a substantial amount of lithium might be consumed during the formation of the solid-electrolyte interphase (SEI) at the negative electrode, which further limits the specific capacity. One potential strategy to enhance the specific capacity could involve upgrading the structural battery electrolyte by incorporating ionic liquids or conducting polymers into the solid phase of the SBE. However, in these instances, the maturity of the updated structural battery electrolyte needs to be individually optimized in detail and should be investigated as a separate case.

2.2. Coulombic Efficiency and Capacity Retention are Achieved Exceptionally Close to 100%

Keeping track of the discharge capacity over a multitude of cycles is a crucial practice that sheds light on several aspects of a

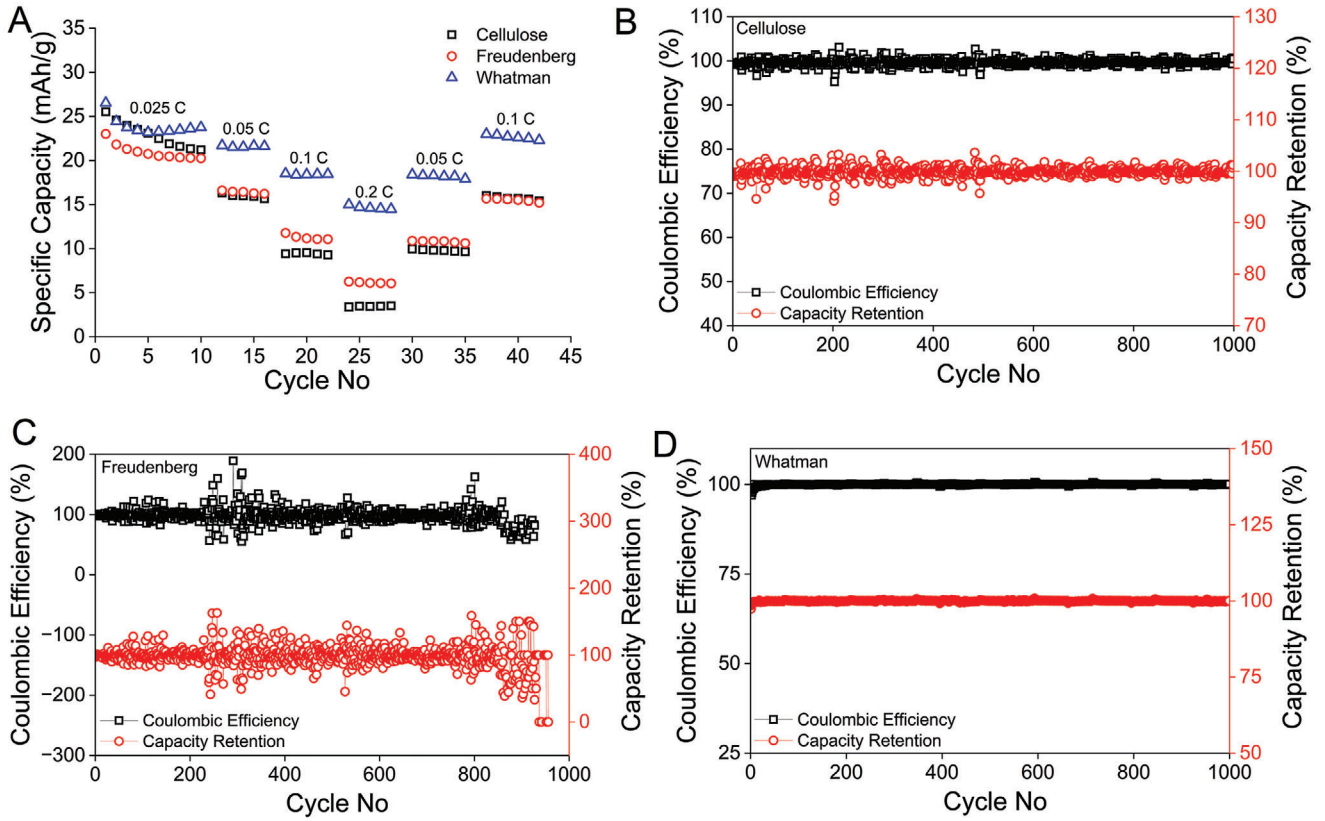

Figure 3. Cyclic stability of all fiber battery. A) Specific capacities at varying C-rate for ten cycles at 0.025C and five cycles for 0.05–0.2C. B–D) Coulombic efficiency and capacity retention of full cell at 0.1C for 1000 cycles. Specific capacity relates to the mass of active materials to allow comparison of the full cell performances. The areal mass loading for positive electrode is 5 and 2.5 mg cm^{-2} for negative electrode.

structural battery performance. This includes the rate at which the battery degrades, its operational efficiency, and the overall health and longevity of the battery. The discharge-specific capacity of all the samples is recorded for up to six cycles at each C-rate (**Figure** 3A). The capacity fades on increasing the C-rate, however, this process is reversible, as the initial capacity is restored when it cycles back at 0.1 and 0.05C after cycling up to a 1C rate. All samples are subjected to long-term cycling stability tests at a 0.1C rate for 1000 cycles. Figure 3B–D represents the capacity retention and Coulombic efficiency for all the structural battery. Capacity Retention is a measure of how well a battery maintains its capacity over time and through numerous charge-discharge cycles. High-capacity retention indicates that the battery can deliver close to its initial capacity even after many cycles, which is crucial for durable and efficient batteries. In this context, the Whatman and cellulose separators, which maintain 100% capacity retention, demonstrate excellent longevity and consistent performance. Coulombic Efficiency, in contrast, assesses the energy efficiency of a battery by measuring the ratio of the total charge extracted from the battery to the total charge inputted over a complete cycle. Achieving 100% Coulombic efficiency signifies that all the energy supplied to the battery can be recovered, reflecting a highly efficient energy conversion process. Here, the Whatman and cellulose separators demonstrate 100% Coulombic efficiency, highlighting their capability for optimal energy conversion and consistent capacity delivery. However, the Freudenberg separator exhibits a decrease in Coulombic efficiency to 90.2% after 860 cycles. Notably, some fluctuations in the Coulombic efficiency of the Freudenberg cell are observed, which are not present in another Freudenberg separator-based cell tested up to 200 cycles (Figure S1, Supporting Information). This decline indicates that some energy is lost during operation, likely due to side reactions or other inefficiencies within the battery system.

2.3. Structural Battery Demonstrates Improved Interface and Reduced Charge Transfer Resistance after 1000 Cycles

The internal resistance across various frequencies in the frequency domain is analyzed using electrochemical impedance spectroscopy (EIS). Voltage excitations are generated, and current responses are measured in potentiostatic mode. After measuring multiple frequencies, the complex impedance can be graphically illustrated in a standard Nyquist plot, where $-Z_{IM}$ is plotted against Z_{RE} as depicted in **Figure** 4A–F. The Nyquist plot offers insight into the underlying mechanisms or phenomena governing an equivalent circuit model system, specific sections here are used to derive equivalent circuit parameters of the structural battery. The purely ohmic internal resistance, represented as R_{Ω} is identified at the frequency where the imaginary part becomes zero. The charge transfer resistance, represented as R_{ct} , is

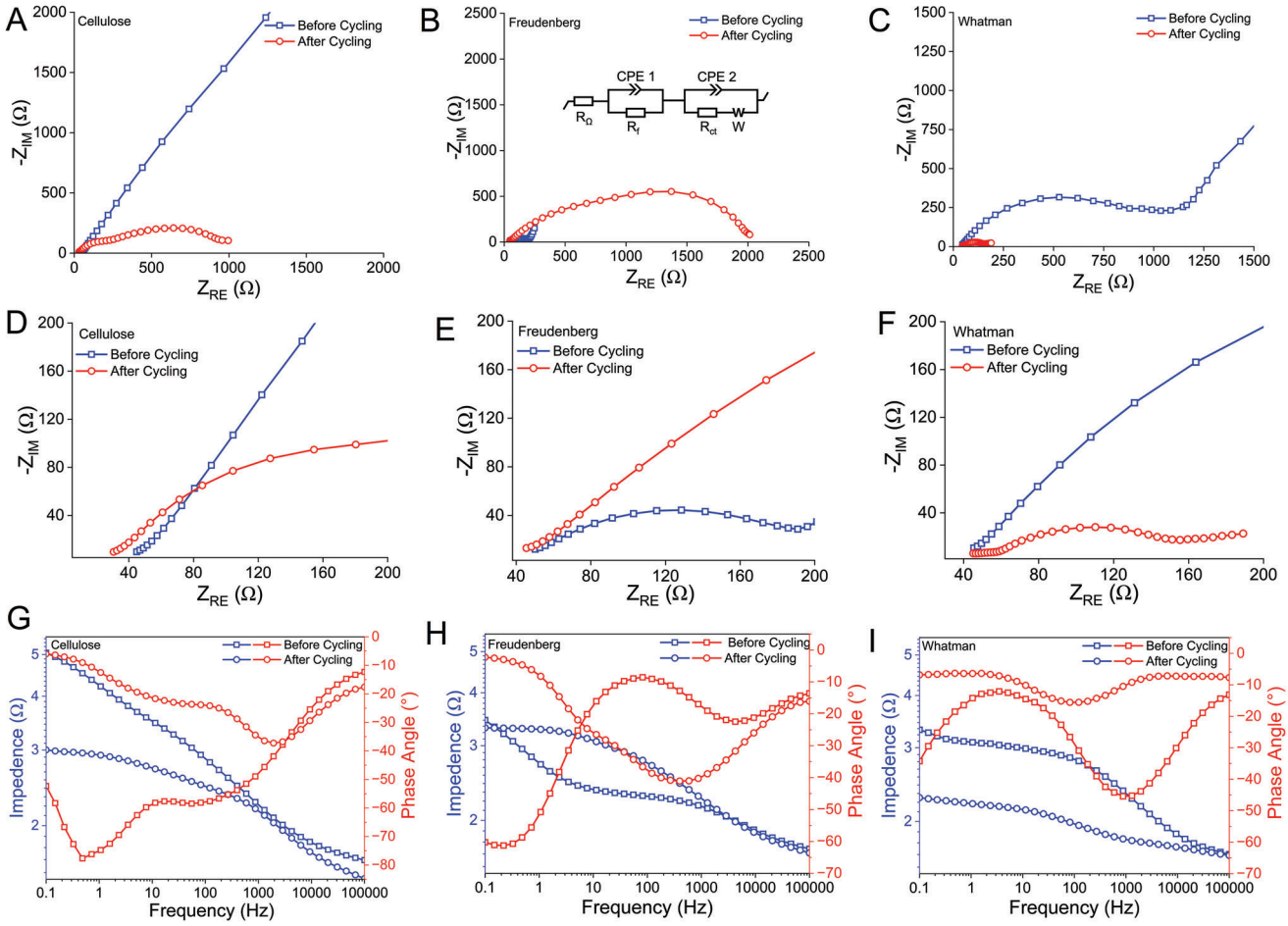

Figure 4. Electrochemical impedance spectroscopy before and after galvanometric cycling at 100 kHz to 100 mHz. A–C) Nyquist plot of full cell with Cellulose, Freudenberg, and Whatman separator, respectively. D–F) Zoomed view of Figure A–C, representing electrode-electrolyte resistance (R_s). G–I) Bode plot of full cell with cellulose, Freudenberg, and Whatman separator, respectively.

derived from the semicircle that spans from the point where the imaginary part is zero to the local minima. This semicircle is fitted with specific equivalent circuit elements. At frequencies below the local minima, the diffusion arc can be adapted to fit with a Constant Phase Element (CPE), such as the Warburg impedance (Z_W). The Warburg impedance is defined by the Warburg coefficient (σ_W) divided by the square root of the angular frequency $\sigma_W/\sqrt{\omega}$. The Bode plot offers distinct advantages in monitoring phase margins, critical for detecting where the system enters a state of instability, characterized by abrupt phase or magnitude changes. Therefore, it proves valuable for gaining deeper insights into structural batteries.

From a mechanistic perspective, the ohmic resistance or bulk internal resistance (R_Ω) of cellulose, Freudenberg, and Whatman separator-based structural battery is observed to be 44, 50, and 64 Ω, respectively before galvanometric cycling. This resistance comes from the battery core components such as the current collector (aluminum and nickel in present case), electrolyte (SBE), and separator. These components contribute solely to resistance without any associated capacitance or inductance effects, and their impact can be seen at Z_{RE}. While bulk resistance remains relatively stable regardless with the state of charge (SOC), prolonged cycling increases the R_Ω due to depletion of lithium ions in structural battery electrolyte. Thus, bulk resistance serves as a reliable indicator for assessing the state of health (SOH) of aged cells. In this scenario, the ohmic resistance drops to 30 Ω for the cellulose battery and 45 Ω for both the Freudenberg and Whatman batteries after they have completed 1000 charge–discharge cycles. This observation affirms the battery's stability and suggests an improvement in the bulk resistance, potentially due to the decrease in surface resistance.

During the initial cycles of a newly assembled structural lithium-ion battery, the electrolyte decomposes at the anode as lithium is consumed. This results in the formation of an insulating layer known as the Solid Electrolyte Interphase (SEI) on the anode surface. The electrode surface acts as a capacitor, with charge accumulation at the interface with the electrolyte ions, forming the double-layer capacitor (C_{dl}). Nevertheless, its properties significantly deviate from those of an ideal capacitor. This non-ideal performance mostly comes from the surface roughness, leakage capacitance, and non-uniform distribution, which can be addressed by incorporating the concept of a Constant Phase Element (CPE) in the modeling of the electrical double layer.[13] Concurrently, charge transfer occurs through a

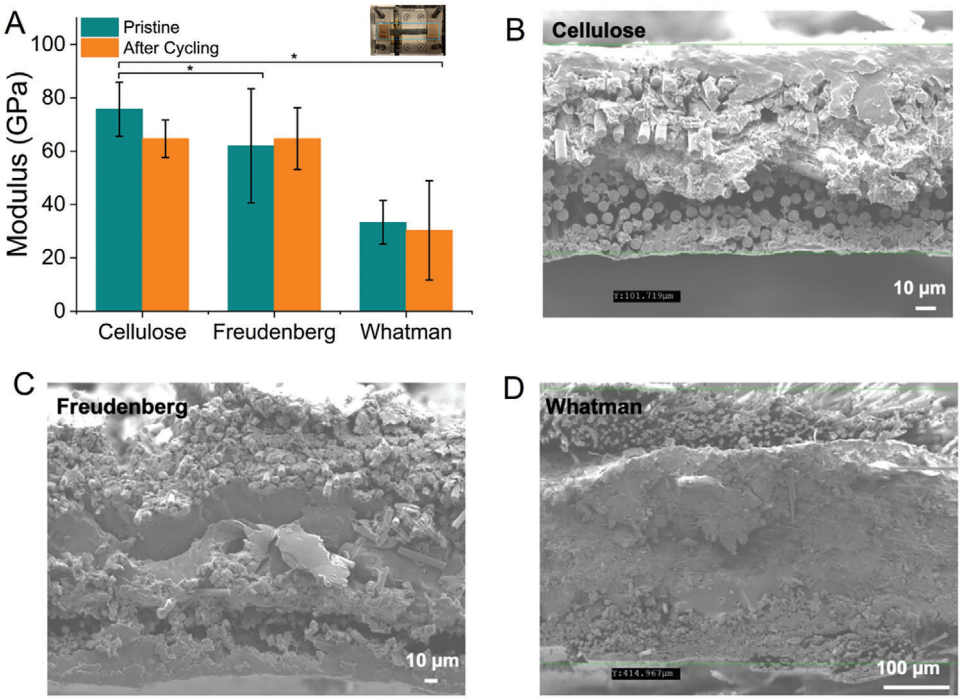

Figure 5. Stiffness and cross-section of all-fiber battery in SBE. A) Modulus of an all-fiber structural battery full cells before and after galvanometric cycling. B–D) SEM cross-section of full cell with varying separators (top, middle, and bottom layer represents the positive electrode, separator, and negative electrode, respectively). Data is presented as mean ± SD, n = 3 and significance is determined by one-way ANOVA, at $p < 0.05$. * denotes a significant difference in the means.

Faraday process, transitioning from electronic to ionic conductivity, which is characterized by charge transfer resistance (R_{ct}). The charge transfer resistance (R_{ct}) is associated with the kinetics of electrochemical reactions and can be influenced by factors such as surface coatings, phase transitions, bandgap structures, particle size, and temperature. The charge transfer resistance (R_{ct}) semicircle is not observed for the cellulose separator before cycling. However, after cycling, the interface between the electrolyte and electrode improves, resulting in the appearance of two merged semicircles, corresponding to an R_{ct} of 940 Ω. The structural battery with the Freudenberg separator shows an R_{ct} of 169 Ω before cycling, which increases to 947 Ω after cycling, leading to decreased cell performance after 950 cycles, as observed during galvanometric cycling (Figure 3C). Conversely, cells with the Whatman separator exhibit an initial R_{ct} of 895 Ω, which decreases to 120 Ω after 1000 charge–discharge cycles.

Additionally, during the charging and discharging processes, lithium ions migrate between the positive and negative electrodes. This mass transport is not instantaneous, leading to additional overpotential. The Warburg resistance (Z_W) quantifies this diffusion phenomenon. Notably, the 45° slope at the low-frequency region is absent for the Freudenberg separator after cycling (Figure 4B,H), indicating poor mass transport. The diameter of the semicircle observed at high frequencies increases significantly, and the slope line corresponding to Warburg impedance at low frequencies vanishes. This indicates a very high charge transfer impedance, suggesting that the electrochemical reactions predominantly occur at the electrode–electrolyte interface, with minimal diffusion of lithium ions within the LFP particles. On the other hand, this inclination associated with Warburg resistance is noticeable in the other samples, which validates improved diffusion of lithium ions within the electrodes. The equivalent circuit, consisting of ohmic resistance (R_Ω), interfacial resistance (R_f), charge transfer resistance (R_{ct}), and Warburg diffusion (W), is presented in the inset of Figure 4B.

2.4. All-Fiber Structural Battery Elastic Modulus Exceeds 76 GPa

The impact of electrochemical cycling on the mechanical performance of structural batteries are evaluated by comparing pristine, uncycled cells with those subjected to 1000 cycles. To assess this, the elastic modulus of structural batteries made with different separators was measured using a tensile test along the fiber direction. The tensile strength of composite materials in the longitudinal direction is predominantly influenced by the strength and volume fraction of the fiber reinforcement. Since the fibers possess significantly higher modulus (294 GPa, T800 Toray) compared to the polymer matrix, they primarily dictate the composite's elastic modulus.[14] Young's modulus is calculated from the linear elastic region of the force-extension curve. The average elastic modulus is calculated using compliance correction method as described in the Experimental Section and represented in **Figure** 5A. Among the structural batteries before cycling, the highest modulus of 76 GPa is observed for the cell with a cellulose separator, which decreases to 62 and 33 GPa for the Freudenberg and Whatman separator, respectively. As anticipated, the modulus of all cycled cells remains relatively stable

(65 GPa for cellulose and Freudenberg, 30 GPa for Whatman) after 1000 electrochemical cycles, given that the longitudinal properties are chiefly controlled by the elastic modulus of the carbon fibers. The Whatman battery shows the lowest elastic modulus since it is the thickest among the separators (which all have very low modulus). The stiff carbon fibers constitute a smaller fraction of the total material (structural battery) due to the separator thickness, which results in lower modulus. Furthermore, poor interfacial adhesion between carbon fibers and separator is observed with Whatman, as the electrodes detach from the separator during the mechanical cutting. The thickness of the cellulose separator-based all-fiber battery (full cell) has been measured at 102 µm (Figure 5B), which is notable for exhibiting the highest modulus among the materials tested, with a value of 76 GPa – indicating its robustness and resilience. In comparison, the all-fiber full cells with Freudenberg and Whatman separators are found to be thicker. The Freudenberg separator-based full cell has a thickness of 120 µm (Figure 5C), while the full cell with the Whatman separator is considerably thicker, measuring 414 µm (Figure 5D). These variations in thickness are crucial as they influence the mechanical properties and performance of the separators in battery applications. The higher modulus of the structural battery cell with the cellulose separator indicates superior stiffness and mechanical strength, which can be beneficial for maintaining structural integrity and enhancing the overall durability of the structural battery. Adding to this, the measurement of strength is not possible due to the limitations of the load cell, which could not exert a high enough force to induce failure in these stiff samples.

The maximum longitudinal strength of the structural battery was assessed both before (pristine) and after electrochemical cycling, with results represented by maximum stress values (Figures S4, Supporting Information). For the optimized pristine cells, the maximum average strengths were 790, 688, and 198 MPa for the cellulose, Freudenberg, and Whatman separator-based full cells, respectively (Figure S4A, Supporting Information). After cycling, these values decreased to 612, 589, and 164 MPa. To evaluate statistical significance, tensile tests were performed on 3–5 specimens per cell type, with the mean values shown in Figure S4B (Supporting Information). It is noteworthy that all cells exhibited high standard deviations, indicating the need for further refinement in the development and characterization of structural batteries.

In addition to separator and mechanical characteristics, the structural stability of the battery materials themselves plays a critical role. During the charging process, the olivine crystal structure of LFP ($LiFePO_4$) transforms into the $FePO_4$ phase, resulting in a theoretical volumetric expansion of 6.77%.[15] However, due to the similar crystal structures of the LFP and $FePO_4$ phases, the volume change during the charging/discharging cycles generates only minimal internal stresses within LFP. Furthermore, the P—O chemical bond is highly stable, preventing the loss of oxygen from the lattice. This stability in crystal structure and minimal internal stress contribute to the overall structural stability and longevity of LFP during cycling.[16]

In contrast, carbon fibers exhibit a reversible longitudinal expansion of 0.6% in structural battery electrolyte (SBE)[17] with a more significant radial expansion of 5–7%.[18] This expansion is particularly concerning because it can induce internal stresses, potentially leading to deformation in multifunctionality, such as causing cracks in the SBE, electrode-SBE interface, coating-SBE interface, or coating-fiber interface. Consequently, examining the morphology of all-fiber batteries after prolonged electrochemical cycling is essential for assessing their performance and durability.[19]

SEM micrographs taken after 1000 cycles (Figure S1, Supporting Information) reveal that the morphology of the cells remains consistent, with no detachment of active materials. Further detailed analysis of the positive electrode's surface at various magnifications, including broad-ion beam (BIB) cross-sections (Figure S2, Supporting Information), indicates that the volume changes in carbon fibers during cycling do not appear to contribute to crack formation. Additionally, the LFP particles on the carbon fiber surface remain stable after 1000 cycles, as no detachment of the LFP active material is observed in the SEM images of the positive electrode (Figures S1B and S2, Supporting Information).

2.5. A Fiber Volume Fraction of 23% has been attained in the Structural Battery

The mechanical properties of composites are dependent on the volume fractions of the carbon fiber and matrix. These fundamental properties can be estimated using the rule of mixtures principle, provided certain assumptions are made.[14,20] The method suggests that the elastic modulus of a composite is essentially a weighted average of the moduli of its two constituents, relying mainly on the volume ratio of the fibers (V_f).[20] The elastic modulus (E_c) of the structural battery composite, composed of carbon fibers (coated and uncoated) and a porous polymer matrix, can be determined by linearly combining the volume fractions and elastic modulus of both the fiber (E_f) and the matrix (E_m) as $E_c = E_f V_f + E_m V_m$, where V_m is the volume fraction of the matrix. This equation is anticipated to be highly accurate, **given** the fibers are sufficiently long to satisfy the assumption of uniform strain. Applying the above assumption and the equation results in a fiber volume fraction of 23% for cellulose-based structural battery cells. The challenge posed by a low volume fraction of fiber can potentially be addressed by minimizing or eliminating the requirement for a separate separator in structural batteries.

2.6. Cellulose-based 102 µm Thin Battery Cell offers the Highest Energy Density of 30 Wh kg^{-1}

A unique balance between energy density and power density is ideally studied using a Ragone plot. Energy density measures the stored energy per unit volume, crucial for long-lasting performance, while power density indicates how quickly energy can be delivered, essential for high-performance applications. Optimizing both in a structural battery ensures efficient energy storage and effective load-bearing capabilities. On an active material basis, which includes the mass of LFP on the positive electrode and CF on the negative electrode, the cellulose-**separator** structural battery can achieve a specific energy density of 72 Wh kg^{-1} at a specific power density of 105 W kg^{-1}. In comparison, the Freudenberg separator attains 75 Wh kg^{-1} at the same power density of 105 W kg^{-1}, and the Whatman separator shows an energy density of 68 Wh kg^{-1} and a power density of 95 W kg^{-1} (**Figure 6A**).

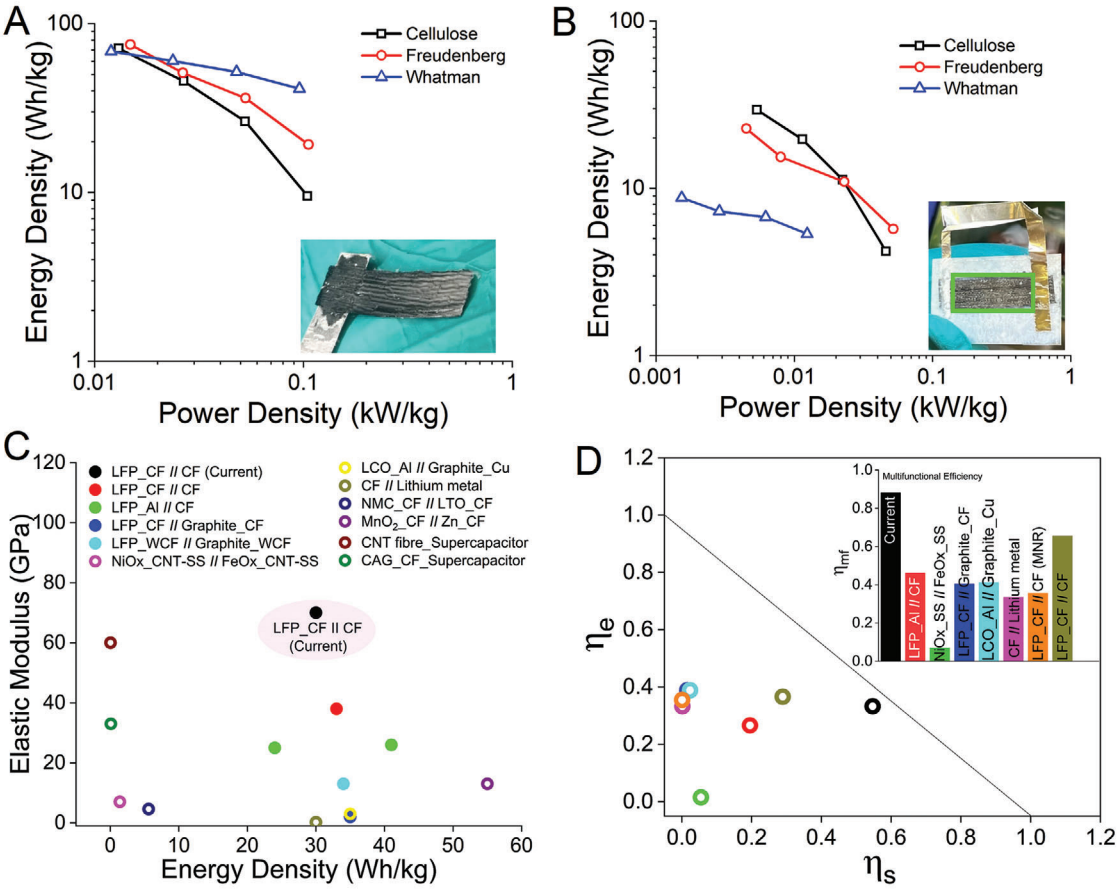

Figure 6. Ragone plot representing the energy and power density of full cell. A) active material-based B) Cell weight based. C) Elastic modulus and energy density of reported structural batteries. D) Multifunctional efficiency matrix of structural batteries. The energy density and elastic modulus data from these reports were used to calculate multifunctional efficiency, η_{mf}. The elastic modulus of the cells is normalized with the modulus of an automotive grade CFRP (128 GPa) to calculate structural efficiency, η_s, and the energy density of the cells is divided by that of a commercial LFP battery (90 Wh kg^{-1}) to calculate the electrochemical efficiency, η_e.

However, it is also crucial to examine the Ragone plot, which considers the mass of the cell. This includes the LFP-coated CF positive electrode, separator, CF negative electrode, and the electrolyte used in the structural battery (the highlighted region in the inset of (Figure 6B). As anticipated, the calculated values for energy and power density decrease when considering the mass of the entire cell. The energy densities for the cellulose, Freudenberg, and Whatman separators are 30, 23, and 9 Wh kg^{-1}, respectively, while the corresponding power densities are 46, 32, and 12 W kg^{-1} (Figure 6B). It is noteworthy that the specific capacity for all separators falls within the 25 mAh g^{-1} range. However, the energy density of the cellulose-separator structural battery is significantly higher due to its low thickness and lightweight nature. Additionally, two critical parameters – modulus and energy density – which are essential for an effective structural battery, are compared with the Lithium Iron Phosphate (LFP) based structural batteries reported in the literature (Figure 6C). The elastic modulus in the current study, at 76 GPa, exceeds all previously reported work. Moreover, it surpasses an energy density of 30 Wh kg^{-1}, thereby significantly advancing the state-of-the-art in structural batteries.

LFP: lithium iron phosphate; CF: carbon fiber; Al: aluminum foil; WCF: woven carbon fabric; CNT-SS: carbon nanotube decorated stainless steel framework; LCO: lithium cobalt oxide; Cu: Copper foil; NMC: lithium nickel manganese cobalt oxide; LTO: lithium-titanium-oxide; CAG: carbon aerogel modified plain weave carbon fiber.

2.7. Multifunctionality of an All-Fiber Structural Battery

The multifunctionality aspect is integrated into each component of the structural battery. The carbon fibers are electrochemically activated in the positive electrodes, serving as current collectors, facilitating electrochemical reactions, and imparting rigidity. The separator prevents short circuits between the positive and negative electrodes, facilitates ion migration, and is impregnated with SBE to enhance durability. The negative electrode, functioning akin to graphite in commercial lithium-ion batteries, stores capacity, acts as a current collector and contributes to mechanical stiffness. The structural battery electrolyte comprises a biphasic solid-liquid electrolyte: the liquid phase transports ions between electrodes, while the solid phase provides mechanical load

transfer via its stiffness, addressing a limitation of traditional liquid-based lithium-ion batteries. This approach allows the achievement of multifunctional properties at the material level.

Evaluation of the multifunctional performance of structural battery composites involves complexities that are not encountered with conventional batteries and structures. A simple performance metric has been proposed to assess the multifunctional efficiency (η_{mf}) of structural batteries, considering both electrochemical efficiency (η_e) and structural efficiency (η_s).[21] The multifunctional efficiency is accessed by $\eta_{mf} = \eta_e + \eta_s$, where η_e corresponds to the ratio of structural battery energy density (30 Wh kg^{-1}, cell mass basis) to that of a standard LFP battery (90 Wh kg^{-1}) and η_s is the elastic modulus of structural battery (76 GPa) to that of a traditional structural component (here, we consider an automotive grade CFRP with a unidirectional modulus of 128 GPa). Thus, a multifunctional efficiency of 0.88 for the best-performing structural battery full cell demonstrated in this study is achieved. A comparison of multifunctional efficiency with devices from the literature is illustrated in Figure 6D, which dictates that the present work achieves the highest η_{mf}. It should be noted that the multifunctional efficiencies reported here do not refer to any real design case. According to this model a multifunctional efficiency, η_{mf}, above unity is needed to realize mass savings. The method is used here to rank materials due to its simplicity and not to analyze potential weight savings in real applications.

A significant challenge in improving multifunctional efficiency remains on the positive electrode side. Previous studies demonstrated $\eta_{mf} > 1$ in half-cell configurations, which do not accurately represent full-cell performance.[12] In a full-cell structural battery configuration, the availability of lithium ions is limited to the structural positive electrode and electrolyte. This availability is further restricted by the inclusion of the solid phase in the structural electrolyte. Additionally, a substantial amount of lithium is typically consumed during the formation of the solid electrolyte interphase (SEI), which limits the energy density of the full-cell structural battery and impacts η_{mf}.

Furthermore, structural batteries offer significant potential for mass savings at the system level compared to traditional monofunctional batteries. However, accurately calculating these potential mass savings for any specific application requires detailed information about the monofunctional components being replaced by the multifunctional material. These calculations consider factors such as mechanical and electrochemical performance, material densities, and other relevant characteristics. For instance, replacing the steel roof of an electric car with a structural battery could result in a 22% weight reduction because parts of the traction battery can be eliminated. On the other hand, substituting the lightweight CFRP hull structure of an electric ferry would yield only about a 10% weight reduction.[4a] The potential for mass savings varies significantly depending on the specific application and the components involved. Understanding these nuances is crucial for optimizing the design and realizing the full benefits of structural batteries in various applications.

3. Conclusion

Structural batteries offer tremendous potential to improve the durability, mobility, and smart functionality in the realm of fully electric systems. By integrating energy storage directly into structural components, these batteries help extend operational endurance, enhance movement capabilities, and enable advanced intelligent features in electric vehicles and other high-tech applications. This study explores the development of multifunctional materials for structural batteries at the material level, demonstrating a functional all-fiber structural battery as proof-of-concept. To create a lighter battery with high energy density, three separators of varying thicknesses were examined. The thinnest separator, made of cellulose at 30 µm, delivers a high energy density of 75 Wh kg^{-1} based on the mass of active materials and 30 Wh kg^{-1} based on cell mass, corresponding to power densities of 105 and 46 W kg^{-1}, respectively. The same structural battery achieves the highest modulus of 76 GPa with an overall 23% carbon fiber volume fraction. The Coulombic efficiency and capacity retention of ≈100% confirms the long-term cycling stability of structural batteries up to 1000 cycles. Advancements in structural batteries have the potential to revolutionize electric power systems and human-machine interaction, paving the way for autonomous operational domains.

4. Experimental Section

Materials: Toray Composite Materials America, Inc. manufactured the T800SC-12K-50C type of Polyacrylonitrile (PAN)-based carbon fibers. These fibers were subsequently converted into ultrathin unidirectional (UD) tapes, ≈15 mm wide, by Oxeon AB in Sweden. MTI Corporation supplied the $LiFePO_4$ powder with an average particle size of 3.5 µm. LayerOne AS in Norway provided the reduced graphene oxide (rGO) containing 95% carbon. Conductive Super P carbon black (CB, ≈40 nm) and polydiallyldimethylammonium chloride (PDDA; 20 wt.% in H_2O) were sourced from Thermo Scientific and Sigma-Aldrich, respectively. Avantor VWR Sweden supplied absolute ethanol (≥99.8%). Sigma-Aldrich provided the Whatman glass microfiber separator (Whatman GF/A, 260 µm thick), while Freudenberg Performance Materials SE & Co. KG, UK, supplied the Freudenberg separator (FS-3002-23, Freudenberg, areal weight of 33 g m^{-2}). Technical Fibre Products Ltd, UK, provided the Fine E glass veil (6 g m^{-2}). NKK Nippon Kodoshi Corp. (Koshi, Japan) generously supplied the cellulose-based NF40-30 separator with a nominal thickness of 30 µm. The bi-continuous structural battery electrolyte (SBE) comprised bisphenol A ethoxylate dimethacrylate (BPAMA) (Mn: 540 g mol-1) monomer from Sartomer Company, Europe, along with the heat-initiator 2,2′-azobis(2-methylpropionitrile) (AIBN), lithium bis(trifluoromethanesulfonyl)imide (LiTFSI, anhydrous 99.99%), propylene carbonate (PC) (PC ≥ 99%, acid <10 ppm, H2O <10 ppm), and ethylene carbonate (EC) (99% anhydrous), all from Sigma-Aldrich. Additionally, PELCO conductive carbon glue, an acrylic binder base used for bonding the current collector and carbon fibers, was purchased from Caspilor, Sweden.

Electrochemical Fabrication of Structural Positive Electrodes: Before proceeding with the synthesis of the positive electrode, the carbon fibers (CF) were subjected to an 8-h reflux desizing process using dichloromethane to remove the polymer sizing. The synthesis of the positive electrodes followed a previously established procedure.[6c,e] Briefly, 500 mg of $LiFePO_4$ powder was dispersed in 50 mL of ethanol using a Sonics VCX-750 Vibra-Cell ultrasonic liquid processor for 20 min. Reduced graphene oxide and carbon black were subsequently added in equal weight ratios (100 mg total) to enhance electrical conductivity and ion transport. The surface charge of $LiFePO_4$ was adjusted by gradually adding 500 µL of PDDA dissolved in 1 mL of ethanol. The solution was then sonicated for an additional 20 min to ensure uniform dispersion of the EPD bath. This final suspension was subjected to cathodic deposition in a two-electrode compartment system, with CF acting as the working electrode parallel to a platinum mesh counter electrode, at a fixed deposition distance of 30 mm. A

constant voltage of 70 V was applied using a Keithley 2450 Sourcemeter for 20 min. The deposited weight was determined after drying the samples at 70 °C for 12 h.

Synthesis of Liquid Electrolyte and Structural Battery Electrolyte (SBE): The SBE mixture was prepared following the reported procedure with slight adjustments under an argon atmosphere and dry conditions (<1 ppm H_2O, <1 ppm O_2).[22] Initially, a stock solution of 1 M liquid electrolyte was made by dissolving 1.0 M LiTFSI in EC:PC 1:1 (50:50 wt.%). For the SBE solution, equal parts of liquid electrolyte and BPAMA monomer were mixed followed by the addition of heat-initiator AIBN (1 wt.% of the BPAMA monomer). The mixture was thoroughly stirred using a vortex to ensure uniformity, then left to degas inside the glovebox before vacuum infusion. The vacuum-infused SBE was subsequently cured in an oven at 90 °C for 45 min.

Vacuum Assisted Resin Infusion for the Manufacturing of Structural Battery Full Cell: A full-cell pouch bag design was used for the manufacturing of structural battery cells. EPD-deposited CF attached to the aluminum current collector was used as positive electrode while pristine CF connected to nickel tabs was used as negative electrode. The electrodes were stacked on each side of an electrically insulating separator and dried in oven at 100 °C overnight. However, in the case of the cellulose separator, the cellulose was dried first at 100 °C for 12 h followed by vacuum drying at 50 °C for 48 h. No, as such treatment was used for Whatman, Freudenberg, and glass-veil. The mass of positive and negative electrode was balanced by considering the deposited LFP on carbon fibers and theoretical capacity of LFP (170 mAh g^{-1}) and CF (372 mAh g^{-1}). The mass of LFP-coated CF in the cathode was 22 mg and the pristine CF in the anode was 11 mg, which corresponds to the areal mass loading of 5 and 2.5 mg cm^{-2}, respectively. A total mass of 33 mg was considered as active material mass in the battery. The structural battery was prepared using a vacuum infusion process, followed by assembly into pouch bag.[6b] Cell components were assembled on a glass plate in the following sequence: 1) placement of release plastic film, 2) positive electrode attached to Al tabs, 3) separator, 4) negative electrode connected to Ni tabs, 5) perforated polyethylene film, 6) breather fabric.

Silicon tubes were connected as inlet and outlet, and whole geometry was sealed with tacky tape and dried in vacuum oven at 50 °C for 12 h before SBE infusion. The SBE was prepared as described above and connected to the inlet tube. The infusion was carried out at a pressure of −0.5 bar, and subsequently cured at 90 °C for 45 min. This results in SBE cured all-fiber structural battery which was sealed inside PET:Al:PE (12 µm:9 µm:75 µm) pouch bag for electrochemical testing. In case of half-cell, similar process was followed for vacuum infusion of positive electrode, while the lithium foil was added right before sealing the pouch bag. An additional 200 µL of liquid electrolyte was added to the pouch bag to facilitate ion conduction.

Electrochemical Testing and Morphological Characterizations of Structural Battery: Cyclic voltammetry (CV), galvanostatic charge/discharge (GCD), and electrochemical impedance spectroscopy (EIS) were conducted using a Bio-Logic SP-300 station. CV of half-cell was performed at a scan rate of 0.1 mV s^{-1} within a voltage range of 2.6 to 4.2 V versus Li/Li^+. GCD cycles were executed across a voltage range of 2–3.6 V at rates from 0.025 to 0.2C for six cycles each, with cycling stability monitored up to 1000 cycles at 0.1C. The selected current for GCD cycling was based on the theoretical capacity of LFP. EIS measurements were carried out over a frequency range from 100 kHz to 100 mHz using an alternating current (AC).

The specific capacity of the samples was determined from discharge curves as per the formula $\boldsymbol{Q = \int Idt/m}$, where Q was the specific capacity in mAh/g based on the deposited active materials mass, I was the current, and m was the mass of the electrodeposited material (g) and dt was the time differential. Specific energy density (ED, Wh/kg) and power density (PD, W/kg) were calculated using following formula: $ED = 1/m_t \int IV\, dt$ and $PD = ED/t_{discharge}$, respectively, where I was the discharging current in Ampere, V was the potential in Volt, m_t was mass of the active material or full cell in kg, and $t_{discharge}$ was the discharge time in hours.

Broad-Ion-Beam Scanning Electron Microscopy (BIB-SEM): Scanning electron microscopy (SEM) of full cells was performed to quantify the thickness of all fiber batteries. SEM was performed using JEOL JSM-7800F Prime model at an acceleration voltage of 5 kV and gold coating of 5 nm. Broad-ion-beam scanning electron microscopy (BIB-SEM) was conducted on cycled positive electrodes. Before examination, the samples were washed in distilled water for 12 h and then dried in a vacuum oven at 60 °C for an additional 12 h. BIB milling was performed using Leica TIC3X with an accelerating voltage of 8 and 6 kV for 6 and 2 h, respectively. Subsequently, the imaging was carried out using a JEOL JSM-7800F Prime SEM.

Tensile Modulus of All-Fiber Structural Battery: For mechanical testing, the SBE-infused LFP-deposited carbon fiber lamina and structural battery full cell were cut into pieces ≈30 mm long and 3 mm wide. Glass fiber tabs were attached to the ends of the lamina using epoxy adhesive films to ensure secure gripping and even load distribution, preventing premature failure or sample slippage. Tensile tests were conducted on at least five samples, with sample thickness measured by SEM. The mechanical testing was performed in tensile mode parallel to the fiber direction using a Deben microtester with a 2.0 kN load cell at a testing speed of 0.2 mm min^{-1}. Strains were derived from the crosshead displacement of the microtester, and the compliance compensation method was used to determine the modulus using ASTM D3379 method which describes the test on single fiber filaments.[10] An apparent modulus, E was calculated using $E = L/CA$, where L was the specimen gauge length, A was the cross-sectional area, and C was the true compliance. The true compliance, C was determined from $C = C_a - C_s$, where C_a was the apparent compliance from the initial linear segment of the load-displacement curve, and C_s was the system compliance, measured experimentally.

Statistical Analysis: All experiments were conducted in triplicate, with the data presented as mean ± SD (n = 3). Statistical significance was determined using one-way ANOVA with Tukey's correction, performed with Origin-Pro 2024 64-bit software, where $p < 0.05$. An asterisk (*) indicates statistical significance.

Supporting Information

Supporting Information is available from the Wiley Online Library or from the author.

Acknowledgements

This research was funded by the Wallenberg Initiative Materials Science for Sustainability (WISE) through the Knut and Alice Wallenberg Foundation. Additional support was provided by the 2DTECH VINNOVA Competence Centre (Ref. 2019-00068), the USAF EOARD (Award No. FA8655-21-1-7038), and the ONR, USA (Award No. N62909-22-1-2037).

Conflict of Interest

The authors declare no conflict of interest.

Data Availability Statement

The data that support the findings of this study are available from the corresponding author upon reasonable request.

Keywords

carbon fiber, electrophoretic deposition, lithium-iron phosphate, structural battery electrolyte, structural lithium-ion batteries

Received: July 7, 2024
Revised: August 26, 2024
Published online: September 10, 2024

[1] a) M. S. Whittingham, Proc. IEEE, IEEE, **2012**, 1518, https://doi.org/10.1109/JPROC.2012.2190170; b) A. Manthiram, *ACS Cent. Sci.* **2017**, *3*, 1063,.

[2] a) D. H. S. Tan, Y.-T. Chen, H. Yang, W. Bao, B. Sreenarayanan, J.-M. Doux, W. Li, B. Lu, S.-Y. Ham, B. Sayahpour, J. Scharf, E. A. Wu, G. Deysher, H. E. Han, H. J. Hah, H. Jeong, J. B. Lee, Z. Chen, Y. S. Meng, *Science* **2021**, *373*, 1494; b) N. A. Chernova, M. F. V. Hidalgo, C. Kaplan, K. Lee, I. Buyuker, C. Siu, B. Wen, J. Ding, M. Zuba, K. M. Wiaderek, I. D. Seymour, S. Britto, L. F. J. Piper, S. P. Ong, K. W. Chapman, C. P. Grey, M. S. Whittingham, *Adv. Energy Mater.* **2020**, *10*, 202002638; c) W. Li, B. Song, A. Manthiram, *Chem. Soc. Rev.* **2017**, *46*, 3006; d) G. M. Hobold, J. Lopez, R. Guo, N. Minafra, A. Banerjee, Y. Shirley Meng, Y. Shao-Horn, B. M. Gallant, *Nat. Energy* **2021**, *6*, 951,

[3] L. E. Asp, S. Leijonmarck, T. Carlson, G. Lindbergh, in 20th Int. Conf. Compos. Mater. (Proc.) Aalborg University, Fredrik Bajers Vej 5, 9100 Aalborg, Denmark Technical University of Denmark, Anker Engelunds Vej 1 Bygning 101A, 2800 Kgs. Lyngby, Denmark, Copenhagen, **2015**, 1121, https://iccm-central.org/Proceedings/ICCM20proceedings/index.htm.

[4] a) W. Johannisson, D. Zenkert, G. Lindbergh, *Multifunct. Mater.* **2019**, *2*, 035002; b) D. Carlstedt, L. E. Asp, *Compos. Part B: Eng.* **2020**, *186*, 107822; c) A. Ishfaq, S. N. Nguyen, E. S. Greenhalgh, M. S. P. Shaffer, A. R. J. Kucernak, L. E. Asp, D. Zenkert, P. Linde, *J. Compos. Mater.* **2022**, *57*, 817.

[5] a) J. F. Snyder, E. L. Wong, C. W. Hubbard, *J. Electrochem. Soc.* **2009**, *156*, A215; b) G. J. H. Lim, K. K. Chan, N. A. A. Sutrisnoh, M. Srinivasan, *Mater. Today Sustain.* **2022**, *20*, 100252.

[6] a) Y. D. Yücel, D. Zenkert, R. W. Lindström, G. Lindbergh, *Electrochem. Commun.* **2024**, *160*, 107670; b) M. S. Siraj, S. Tasneem, D. Carlstedt, S. Duan, M. Johansen, C. Larsson, J. Xu, F. Liu, F. Edgren, L. E. Asp, *Adv. Energy Sustain. Res.* **2023**, *4*, 2300109; c) J. S. Sanchez, J. Xu, Z. Xia, J. Sun, L. E. Asp, V. Palermo, *Compos. Sci. Technol.* **2021**, *208*, 108768; d) M. H. Kjell, E. Jacques, D. Zenkert, M. Behm, G. Lindbergh, *J. Electrochem. Soc.* **2011**, *158*, A1455,; e) Z. Xia, Z. Li, J. Xu, S. Sasidharan, J. S. Sanchez, V. Palermo, L. E. Asp, *Compos. Sci. Technol.* **2024**, *251*, 110568.

[7] J. Hagberg, H. A. Maples, K. S. P. Alvim, J. Xu, W. Johannisson, A. Bismarck, D. Zenkert, G. Lindbergh, *Compos. Sci. Technol.* **2018**, *162*, 235.

[8] a) E. Jacques, M. H. Kjell, D. Zenkert, G. Lindbergh, *Carbon* **2014**, *68*, 725; b) E. Jacques, M. H. Kjell, D. Zenkert, G. Lindbergh, M. Behm, M. Willgert, *Compos. Sci. Technol.* **2012**, *72*, 792.

[9] K. Moyer, C. Meng, B. Marshall, O. Assal, J. Eaves, D. Perez, R. Karkkainen, L. Roberson, C. L. Pint, *Energy Storage Mater.* **2020**, *24*, 676.

[10] L. E. Asp, K. Bouton, D. Carlstedt, S. Duan, R. Harnden, W. Johannisson, M. Johansen, M. K. Johansson, G. Lindbergh, F. Liu, *Adv. Energy Sustain. Res.* **2021**, *2*, 2000093.

[11] K. Bouton, L. Schneider, D. Zenkert, G. Lindbergh, *Compos. Sci. Technol.* **2024**, *256*, 110728.

[12] R. Chaudhary, A. Chetry, J. Xu, Z. Xia, L. E. Asp, *Adv. Sci.* **2024**, *11*, 2404012.

[13] a) W. Choi, H.-C. Shin, J. M. Kim, J.-Y. Choi, W.-S. Yoon, *J. Electrochem. Sci. Technol.* **2020**, *11*, 1; b) S. Rodrigues, N. Munichandraiah, A. K. Shukla, *J. Solid State Electrochem.* **1999**, *3*, 397.

[14] T. W. Clyne, D. Hull, *An Introduction to Composite Materials*, Cambridge University Press, Cambridge, England, **2019**.

[15] W.-J. Zhang, *J. Power Sources* **2011**, *196*, 2962.

[16] L. Yang, K. Yang, J. Zheng, K. Xu, K. Amine, F. Pan, *Chem. Soc. Rev.* **2020**, *49*, 4667.

[17] D. Carlstedt, F. Rittweger, K. Runesson, A. M. Navarro-Suárez, J. Xu, S. Duan, F. Larsson, K.-R. Riemschneider, L. E. Asp, *Compos. Sci. Technol.* **2022**, *220*, 109283.

[18] S. Duan, A. H. Iyer, D. Carlstedt, F. Rittweger, A. Sharits, C. Maddox, K.-R. Riemschneider, D. Mollenhauer, M. Colliander, F. Liu, *Carbon* **2021**, *185*, 234.

[19] J. Xu, J. Varna, *J. Compos. Mater.* **2019**, *53*, 3615.

[20] K. K. Chawla, *Composite Materials: Science and Engineering*, Springer Science & Business Media, New York, **2012**.

[21] a) J. Snyder, E. Gienger, E. Wetzel, *J. Compos. Mater.* **2015**, *49*, 1835; b) N. A. A. Sutrisnoh, G. J. Lim, K. K. Chan, J. N. Lim, M. Srinivasan, *Compos. Sci. Technol.* **2023**, *242*, 110147; c) J. Snyder, D. O'Brien, E. D. Wetzel, in *Handbook of solid state batteries*, World Scientific, **2016**, pp. 657–699, https://doi.org/10.1142/9789814651905_0019.

[22] L. M. Schneider, N. Ihrner, D. Zenkert, M. Johansson, *ACS Appl. Energy Mater.* **2019**, *2*, 4362.